

Electrochemistry-Driven Complete Reconstruction of Spent Lithium-Ion Battery Cathodes for Matter Recycling

Yu Wang, Sicheng Feng, Junling Huang, Yuan Feng, Kai Luo, Fang Liu, Shidong Li,*
Xuanpeng Wang, and Jiashen Meng*

The rapid expansion of lithium-ion batteries (LIBs) applications has created urgent recycling challenges. To tackle these issues, this study proposes a novel electrochemistry-driven complete reconstruction (EDCR) strategy for effective recycling of cathode materials. The well-designed electrochemical cell is based on a used aluminum foil anode and spent cathodes in a tamed chloroaluminate molten salt electrolyte. During the discharge process, the spent cathodes undergo a reduction reaction, converting high-valence transition metals into their elemental forms. After deep discharge, the spent LiCoO_2 cathode completely decomposes into Co , LiCl , and Al_2O_3 . Subsequent treatment involving washing and calcination produces a pure LiCl solution and a

mixed solid of Co_3O_4 and Al_2O_3 , which can be used to synthesize new cathode materials directly. Experimental results demonstrate the versatility of this method, achieving high recovery rates for LiCoO_2 , ternary cathodes (including NCM811 and NCA), as well as lithium–iron phosphate (LiFePO_4). When compared to traditional pyrometallurgical and hydrometallurgical methods, the EDCR strategy notably lowers energy consumption by 23% and reduces greenhouse gas emissions, all while ensuring a streamlined workflow, reduced operational costs, and a competitive profit margin of \$1.96 per kilogram of batteries processed. This work paves the way for a sustainable closed-loop LIB resource recovery.

1. Introduction

Since their introduction to the market in 1991, lithium-ion batteries (LIBs) have transformed energy storage technologies worldwide.^[1,2] With an impressive energy density of 250–300 Wh kg^{-1} —significantly higher than lead-acid batteries (30–50 Wh kg^{-1}) and nickel-metal hydride batteries (70–100 Wh kg^{-1})—as well as excellent cycle stability (over 80% capacity retention after 1000 charge-discharge cycles) and a long lifespan of 8 to 15 years, LIBs have become essential in consumer electronics, electric vehicles (EVs), and renewable energy systems.^[3–6] In the last decade, the global

shift toward sustainable energy has accelerated the adoption of LIBs across various applications. For instance, global EV sales rose from 3.2 million units in 2020 to 10 million units in 2023, resulting in a 200% increase in demand for traction batteries. At the same time, government initiatives aimed at achieving carbon neutrality have facilitated the widespread installation of grid-scale energy storage systems, with LIBs representing 90% of the 45 GWh of newly installed global storage capacity in 2022.^[7,8] Despite this rapid growth, a significant challenge has emerged: the rapid accumulation of spent LIBs, particularly as early-generation EV batteries approach the end of their typical lifespan of 8 to 10 years. The International Energy Agency (IEA) estimates that annual waste from EV batteries will surpass 4 million metric tons by 2040, and total global LIB waste could reach 12 million metric tons when accounting for consumer electronics and stationary storage systems.^[9,10] Improper disposal of these batteries not only wastes valuable metals, including lithium, cobalt, and nickel but also presents serious environmental risks, such as toxic leachate and soil contamination.^[11,12] For example, cobalt mining in the Democratic Republic of the Congo (DRC) has caused severe ecological damage and labor rights abuses, while lithium extraction in the “lithium triangle” (comprising Chile, Argentina, and Bolivia) encounters increasing geopolitical risks that threaten supply chain stability. Additionally, the leakage of battery electrolytes (such as LiPF_6) and heavy metals (like cobalt and nickel) can produce toxic leachates that contaminate both soil and groundwater. Research shows that the improper disposal of a single 20 kg EV battery can release enough heavy metals to render one hectare of agricultural land infertile for up to 50 years.^[13,14] Concurrently, the rising production of batteries is putting pressure on the supply chain for critical materials, leading to shortages of lithium salts and transition metals that hinder industry growth.^[15,16] These imbalances between supply and demand

Y. Wang, S. Feng, Y. Feng, K. Luo, F. Liu, J. Meng

State Key Laboratory of Advanced Technology for Materials Synthesis and Processing

School of Materials Science and Engineering

Wuhan University of Technology

Wuhan, Hubei 430070, China

E-mail: jsmeng@whut.edu.cn

Y. Wang, S. Li, X. Wang, J. Meng

Hubei Longzhong Laboratory

Wuhan University of Technology (Xiangyang Demonstration Zone)

Xiangyang, Hubei 441000, China

E-mail: lsd_jelly1993@163.com

J. Huang, X. Wang

Department of Physical Science & Technology

School of Physics and Mechanics

Wuhan University of Technology

Wuhan, Hubei 430070, China

X. Wang, J. Meng

Zhongyu Feima New Material Technology Innovation Center (Zhengzhou) Co., Ltd.

Zhengzhou, Henan 450001, China



Supporting information for this article is available on the WWW under <https://doi.org/10.1002/batt.202500113>

have resulted in significant cost increases, highlighting the urgent need for sustainable recycling strategies to address resource depletion and reduce environmental damage.^[17,18] As a result, developing innovative recycling strategies that balance economic feasibility, environmental sustainability, and material versatility has become essential in addressing the twin crises of resource scarcity and environmental degradation.^[19–21]

Among the components of spent LIBs, cathode materials are the most economically valuable due to their high concentrations of critical metals such as lithium, cobalt, and nickel.^[12,22] Current recycling technologies for recovering these metals can be categorized into three main types: pyrometallurgical, hydrometallurgical, and biometallurgical methods, which are often used in hybrid combinations.^[23] The pyrometallurgical method, which is the most widely used in industry, involves high-temperature smelting (over 1400 °C) to convert cathode materials into alloy phases.^[9] However, this process has significant drawbacks, including high energy consumption, emissions of toxic gases (such as dioxins and hydrofluoric acid), and incomplete recovery of lithium due to its volatility, resulting in residual lithium being trapped in slag byproducts. Hydrometallurgical methods can achieve high metal leaching rates (over 95%) and purity through acid digestion using reagents like hydrochloric acid, nitric acid, and sulfuric acid. However, these methods also encounter environmental and safety issues related to corrosive chemicals and wastewater management.^[24–26] The biometallurgical approach provides a cost-effective alternative by utilizing acids produced by microorganisms to leach metals. Despite its economic advantages, this method is hindered by slow reaction rates (ranging from weeks to months) and the toxicity of heavy metals in cathodes, which affects bacterial viability and limits its scalability for industrial applications.^[27,28] Researchers are exploring innovative strategies for recycling spent LIB cathodes, including relithiation processes aimed at directly regenerating degraded cathode materials.^[29–33] For example, Xi et al. introduced a benzoate salt with a special molecular configuration into the molten salt by improving the molten salt method, which facilitated the rapid Li⁺ transport to the surface of spent LiNi_{0.5}Co_{0.2}Mn_{0.3}O₂ through a quasi-Grotthuss topochemical mechanism, thereby significantly improving the prelithiation and repair efficiency of spent LIB cathodes.^[34] Nonetheless, a considerable number of studies continue to focus primarily on developing new leaching systems for extracting valuable metals from cathodes.^[35] For instance, deep eutectic solvents have shown potential as an effective medium for extracting critical metals from spent cathodes; however, these methods still face ongoing challenges, such as suboptimal leaching efficiency and unresolved environmental issues regarding solvent toxicity and waste disposal.^[36–40] These challenges highlight the urgent need for innovative recycling strategies that balance efficiency, environmental sustainability, and economic feasibility to tackle the dual crises of resource scarcity and battery waste.^[41]

High-temperature molten salts, known for their excellent ionic conductivity, fast reaction kinetics, and wide electrochemical stability ranges, have been widely applied in energy storage, material synthesis, and metal extraction.^[42–46] Utilizing these advantageous properties, we have developed an electrochemistry-driven

complete reconstruction (EDCR) method for recycling spent LIB cathodes. This process utilizes a tamed quaternary molten salt system as the electrolyte, where the modulation of Lewis acidity and basicity allows for the regulation of metal solubility and enables selective separation. In this method, spent LIB cathodes (such as LiCoO₂) are disassembled, with the active materials and aluminum foil being repurposed as cathode and anode electrodes, respectively. Under full discharge conditions (5 mA g⁻¹, 180 °C), spent LiCoO₂ is entirely electrochemically reconstructed into lithium chloride (LiCl), metallic cobalt (Co), and aluminum oxide (Al₂O₃). Following this, water washing isolates the LiCl, and subsequent calcination in air condition transforms residual solids into a Co₃O₄/Al₂O₃ mixture, which can be directly used to synthesize new cathode materials. The EDCR method shows broad applicability, successfully recovering ternary cathodes such as NCM811 and NCA, as well as LiFePO₄, with discharge capacities of 718, 790, and 278 mAh g⁻¹, respectively. In comparison to traditional pyrometallurgical and hydrometallurgical methods, the EDCR eliminates the use of corrosive reagents and high-temperature smelting (above 1400°C), leading to a 23% reduction in energy consumption and a 35% decrease in greenhouse gas emissions. This streamlined and environmentally friendly approach achieves a competitive profit margin of \$1.96 per kilogram of processed batteries, positioning it as a scalable solution for sustainable battery recycling.

2. Results and Discussions

2.1. Operation Process and Mechanism of the EDCR Strategy

The operation process of our EDCR strategy is illustrated in Figure 1a. The process begins with the disassembly of spent LIB to extract used cathode materials. Through an interfacial chemistry (Figure S1, Supporting Information), the active cathode material is separated from the aluminum current collector. The retrieved cathode material is subsequently ball-milled to produce fine particles measuring 4 to 8 micrometers (Figure S2, Supporting Information), which are then repurposed as the cathode electrode; flattened aluminum foil is used as the anode. A quaternary molten salt system consisting of AlCl₃, KCl, NaCl, and LiCl was prepared with the molar ratio of AlCl₃ to alkali metal chlorides (A_{Cl}, A = K/Na/Li) set at 0.95, and the specific ratio of AlCl₃:NaCl:LiCl:KCl was 0.95:0.43:0.42:0.15, to form molten salt aluminum batteries. The electrolyte is composed of a slight excess of alkali metal chlorides, and the battery operates at a temperature of 180 °C. LiCoO₂ (LCO) is chosen as the model system for its high economic value; full discharge at a rate of 5 mA g⁻¹ facilitates the complete electrochemical reconstruction of LCO (illustrated in Figure 1b). Unlike the acidic chloroaluminate electrolyte environment where Al is mainly supplied by the reversible conversion of Al₂Cl₇⁻ and AlCl₄⁻, in the basic molten salt electrolyte, it is mainly AlCl₄⁻ coexisting with Cl⁻.^[47–50] At the cathode, the AlCl₄⁻ anion displaces Li⁺ and Co²⁺ from LCO by electrochemical processes and generates Al₂O₃ and in basic molten salts Co²⁺ ions can gain electrons in subsequent electrochemical processes to be deposited to the cathode side as metallic Co, whereas Li⁺ exists in the form of LiCl after coordination with Cl⁻ (Equation 1). Concurrently, Al stripping

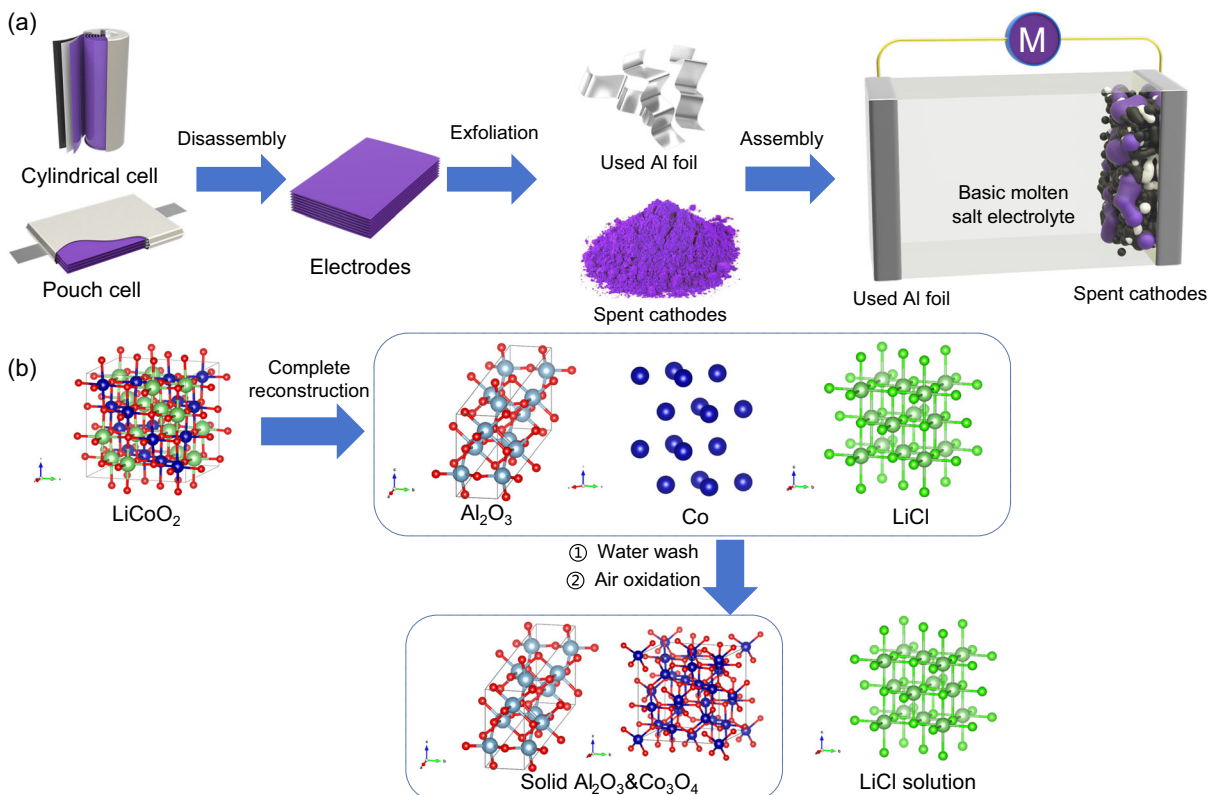
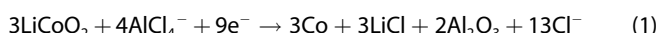


Figure 1. a) Schematic diagram of the recycling process for spent LCO cathode materials. The process begins with the disassembly of the LIB, where the cathode is separated into spent cathode materials and Al foil. These components are then used to assemble an alkaline molten salt Al-LCO battery. b) Schematic diagram of the EDCR process. Through a complete discharge process, the LCO is reconstructed and transformed into LiCl, Co, and Al₂O₃. The products are separated via water washing and calcination into a LiCl solution and a solid mixture of Al₂O₃ and Co₃O₄.

occurs at the anode (Equation 2). The overall reaction during discharge is summarized in Equation 3.

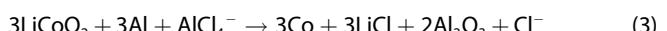
Cathode reaction



Anode reaction



Overall reaction



After the electrochemical reaction, the resulting products undergo aqueous washing and filtration to isolate LiCl in the dissolved phase, achieving a lithium recovery rate of over 95%. The remaining solid precipitate is then calcined in ambient air at 350 °C, resulting in a homogeneous mixture of Al₂O₃ and Co₃O₄. This calcined composite acts as a precursor for the synthesis of high-performance cathode materials, thereby facilitating closed-loop resource utilization.

2.2. Characterizations of the Derived Products During EDCR

Figure 2a displays the discharge profile of an Al-LCO cell operating in a basic molten salt electrolyte at 180 °C. The LCO cathode achieves a specific capacity of 763 mAh g⁻¹ under a current

density of 5 mA g⁻¹, which is 93% of its theoretical capacity of 818 mAh g⁻¹. This validates the complete electrochemical reconstruction of LiCoO₂ into metallic Co, LiCl, and Al₂O₃. X-ray diffraction (XRD) analysis of the fully discharged cathode material (Figure 2b) indicates the complete disappearance of the (003) diffraction peak of LiCoO₂, confirming its structural decomposition.^[51] The newly formed phases are clearly identified as metallic Co (PDF #05-0727) and LiCl (PDF #04-0664), providing direct evidence of the total electrochemical reconstitution of LCO into Co, LiCl, and Al₂O₃. Analysis of the hysteresis loop before and after the reaction reveals that the spent LCO cathode material is essentially non-magnetic prior to full discharge. However, after discharge, the product exhibits significant magnetism, indicative of the formation of magnetic Co (Figure 2c and S3, Supporting Information). Magnetic hysteresis measurements show that the spent LiCoO₂ cathode has negligible magnetism before discharge, which is consistent with its nonmagnetic layered oxide structure. After full discharge, the product exhibits clear ferromagnetic behavior, with a remanent magnetization of 15 emu g⁻¹, which is directly attributed to the formation of metallic cobalt. Transmission electron microscopy (TEM) imaging (Figure 2d) reveals the formation of densely packed crystalline nanoparticles on the discharged cathode surface. Lattice indexing confirms the presence of both LiCl and metallic Co nanoparticles, with distinct lattice fringes that correspond to their crystallographic orientations. Specifically, LiCl domains exhibit

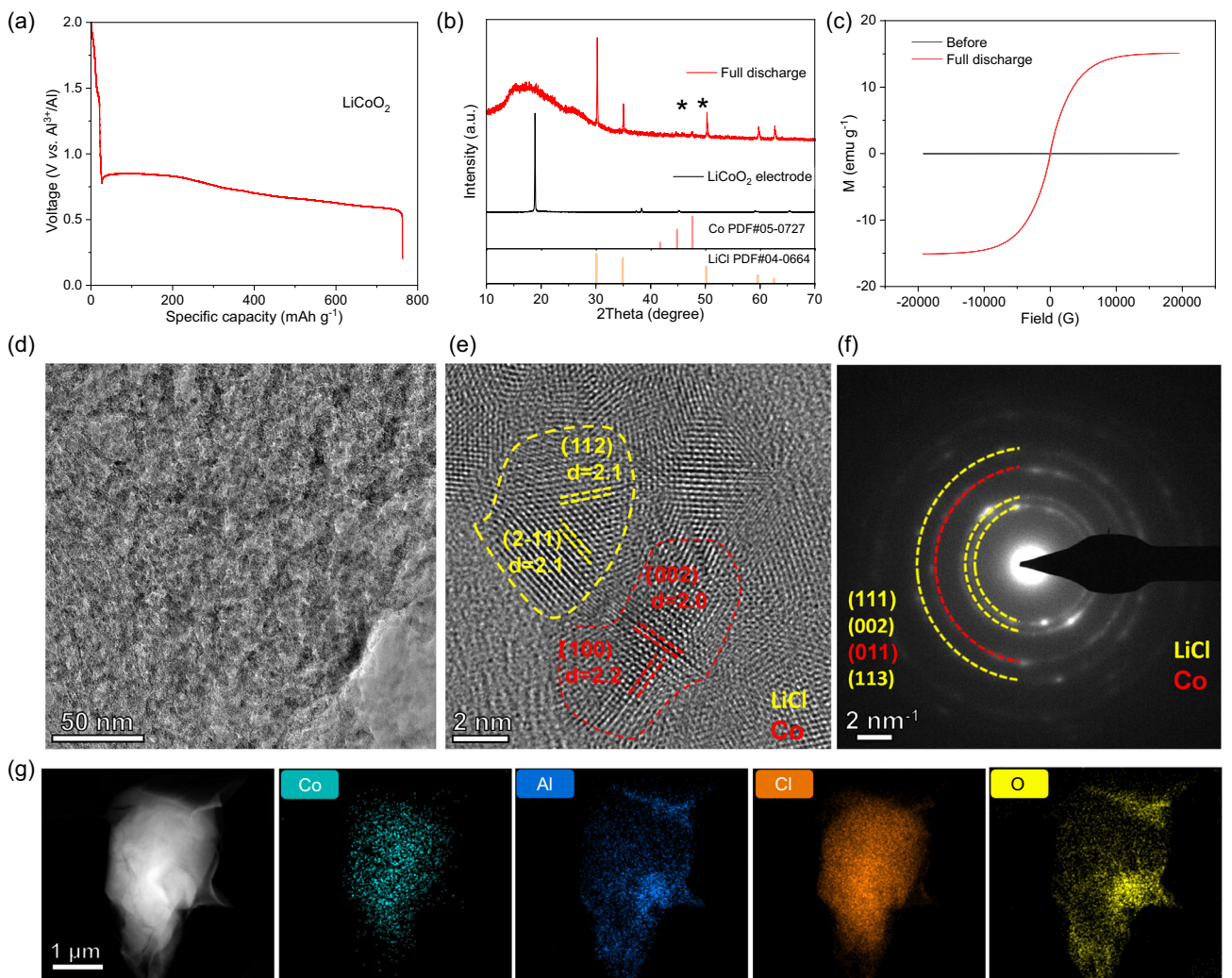


Figure 2. Characterizations of the spent LCO before and after full discharge. a) Typical discharge curve of the Al-LCO batter at an operation temperature of 180 °C with a discharge current density of 5 mA g⁻¹. b) XRD pattern of the spent LCO after full discharge. c) Hysteresis loops of the spent LCO before and after full discharge. d,e) TEM images of the spent LCO after full discharge. f) SAED pattern of the spent LCO after full discharge. g) HAADF-STEM images and EDS maps of the spent LCO after full discharge.

ordered fringes with a spacing of 0.21 nm, matching the (2̄1) and (112) planes (PDF #04-0664), while Co nanoparticles show spacings of 0.20 and 0.22 nm, corresponding to the (002) and (100) planes of metallic Co (PDF #05-0727) (Figure 2e). Selected-area electron diffraction (SAED) patterns (Figure 2f) further validate the multiphase structure, with diffraction rings indexed to the (111), (002), and (113) planes of LiCl and the (011) plane of Co. Figure 2g and S4, Supporting Information, present the high-angle annular dark field scanning transmission electron microscopy (HAADF-STEM) image along with the corresponding elemental maps of the discharged product. The signals for Co and Cl show a homogeneous spatial distribution, confirming the uniform dispersion of LiCl and Co nanocomposites as the primary reaction products. In contrast, the elemental signals of Al and O do not show a homogeneous distribution as in the case of Co and Cl, but instead show a very pronounced spatial overlap, which also favorably demonstrates the presence of amorphous Al₂O₃ in the product. This phase-separated structure is consistent with the EDCR mechanism, in which LiCl and metallic Co are selectively

reconstituted, while residual Al³⁺ reacts with oxygen to form amorphous Al₂O₃ as a secondary phase.

To eliminate any potential interference from LiCl in the electrolyte, we assembled six Al-LCO cells with nearly identical electrode masses. Under testing conditions at 180 °C, three of the cells were fully discharged, while the other three were kept in static incubation for the same duration. After disassembling the cells, the electrodes were washed under identical aqueous conditions. Inductively coupled plasma (ICP) analysis of the washing solutions showed significantly higher lithium concentrations in the solutions from fully discharged electrodes (37 ppm) compared to those from nondischarged electrodes (4 ppm). This finding clearly indicates that the LiCl present in the products primarily results from the complete reconstruction process, rather than contamination from residual electrolyte (see Figure S5, Supporting Information).

Furthermore, the washed product was calcined at 350 °C in air condition, resulting in the formation of the final product. XRD analysis (Figure 3a) reveals that indicates that the final product primarily consists of Co₃O₄, showing strong diffraction peaks at the

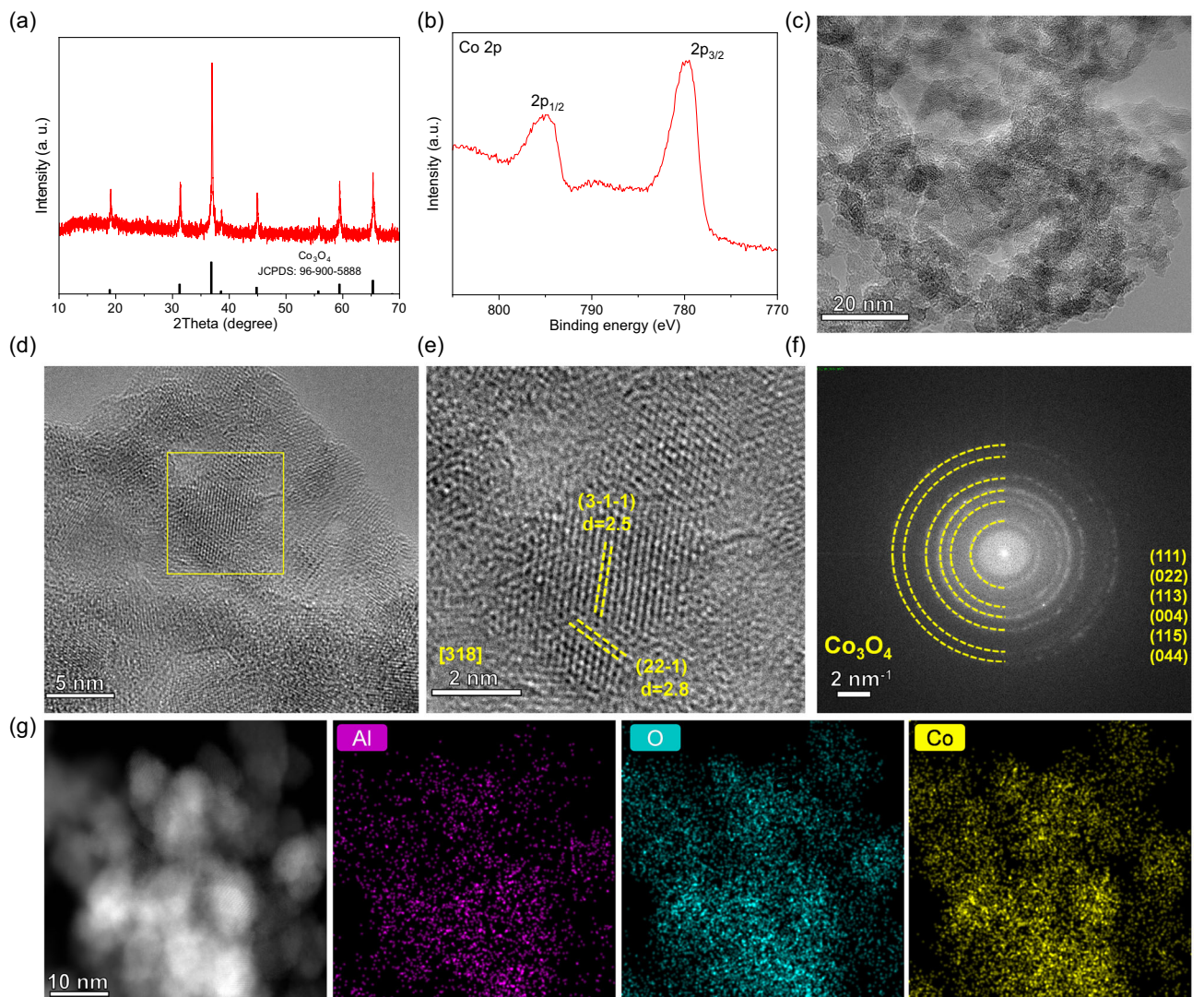


Figure 3. Characterizations of the final product. a) XRD pattern of the products. b) Co 2p XPS spectrum of the products. c-e) TEM images and corresponding magnified views of the final product. f) SAED pattern of the products. g) HAADF-STEM images and EDS maps of the final product.

(111), (220), (311), and (400) crystal planes that match the standard Co_3O_4 phase (PDF #42-1467). The chemical valence states of cobalt in the calcined product were examined using X-ray photoelectron spectroscopy (XPS). As shown in Figure 3b, the Co 2p spectrum exhibits two major peaks at binding energies of 779.6 eV (Co 2p_{3/2}) and 795.1 eV (Co 2p_{1/2}), along with satellite features characteristic of Co³⁺ and Co²⁺ oxidation states. These spectral characteristics align with the mixed-valence configuration of Co_3O_4 ($\text{Co}^{2+}[\text{Co}^{3+}]_2\text{O}_4$), confirming that the spinel Co_3O_4 phase is predominant in the final product. TEM analysis (Figure 3c,d) reveals that the calcined product comprises agglomerated crystalline nanoparticles with an average diameter of 5 nm. Lattice fringe analysis (Figure 3e) identifies spacings of 0.25 and 0.28 nm, corresponding to the (3̄1̄1) and (22̄1̄) planes of the spinel Co_3O_4 phase (PDF #42-1467). SAED patterns (Figure 3f) further confirm the Co_3O_4 structure, with diffraction rings indexed to the (111), (022), (113), (004), (115), and (044) crystal planes. HAADF-STEM image and elemental mapping (Figure 3g) show that the calcined samples exhibit agglomerates of particles smaller than 10 nm, as well

as a homogeneous distribution of the elements Al, Co, and O in them. A closer look reveals that the O elemental signals overlap very much with both Al and Co, and there is a small amount of noncorrespondence between the elemental signals of Co and Al, which further proves the simultaneous presence of Co_3O_4 and Al_2O_3 in the calcined product. The overlap of Al and O signals, along with the lack of crystalline Al_2O_3 diffraction peaks in the XRD analysis, suggests the presence of amorphous Al_2O_3 domains. These results demonstrate that the calcined product is a nanocomposite containing crystalline Co_3O_4 nanoparticles embedded in an amorphous Al_2O_3 matrix, confirming the effectiveness of the EDCR process in achieving phase-selective reconstruction.

To systematically assess the factors influencing material conversion efficiency during the electrochemical reconstruction process, we examined the effects of operating temperature, current density, and cathode particle size on discharge performance. The extent of LiCoO_2 reconstruction was measured by comparing the discharge capacities of Al-LCO molten salt batteries under different conditions. Initially, we explored how temperature

affects the complete reconstruction process. Under a constant discharge current density of 5 mA g^{-1} , reducing the reaction temperature from 180 to 150°C led to a decrease in discharge capacity from 763 to 698 mAh g^{-1} (an 8.5% reduction), indicating slower reaction kinetics and partial inhibition of complete reconstruction at lower temperatures (Figure S6a, Supporting Information). XRD analysis of the final product confirmed that the characteristic peaks remained predominantly consistent with the Co_3O_4 phase (PDF #42-1467) (Figure S6b, Supporting Information). Next, we examined the influence of current density. Increasing the current density from 5 to 10 mA g^{-1} under identical conditions led to a slight capacity reduction to 715 mAh g^{-1} (6.3% decrease), suggesting partial polarization effects under higher current loads (Figure S7a, Supporting Information). XRD patterns of the resulting product continued to show strong alignment with the Co_3O_4 phase, confirming the structural integrity of the reconstructed material. Finally, we assessed the impact of particle size (Figure S7b, Supporting Information). Employing unmilled LiCoO_2 particles ($10\text{--}25 \mu\text{m}$, Figure S2a,b, Supporting Information) without changing other parameters resulted in a significant capacity drop to 305 mAh g^{-1} (a 60% reduction) (Figure S8a, Supporting Information). This decline is attributed to limited solid-liquid interfacial contact and extended diffusion paths in larger particles. XRD analysis of the resulting product revealed partial conformity to the Co_3O_4 phase, while the (003) diffraction peak characteristic of pristine LiCoO_2 remained prominent, indicating incomplete reconstruction due to inadequate particle refinement (Figure S8b, Supporting Information). These results underscore the crucial role of nanoscale particle size ($4\text{--}8 \mu\text{m}$ postball milling) in enhancing interfacial reactivity and achieving complete phase reconstruction. This EDCR strategy demonstrates resilience to moderate variations in temperature and current density but is highly sensitive to particle morphology, highlighting the need for mechanical pretreatment to ensure efficient resource recovery.

2.3. Wide Adaption for Other Spent Cathode Materials

To confirm the universality and industrial relevance of the EDCR strategy, it is essential to apply it beyond LCO to other widely used cathode materials. Commercial LIBs utilize various cathode materials designed for specific applications, such as high-nickel layered oxides for EVs that require high-energy density, and lithium–iron phosphate (LiFePO_4 , LFP) for cost-sensitive grid storage systems.^[45,52,53] Following the successful application of the molten salt EDCR method to spent LCO cathodes, we explored its potential for recycling other commercial LIB cathode materials, such as $\text{LiNi}_{0.8}\text{Co}_{0.1}\text{Mn}_{0.1}\text{O}_2$ (NCM811), $\text{LiNi}_{0.85}\text{Co}_{0.1}\text{Al}_{0.05}\text{O}_2$ (NCA) and LFP. According to the established protocol for LCO recycling (Figure S9–S11, Supporting Information), these spent cathode materials underwent ball milling to achieve a particle size of $4\text{--}8 \mu\text{m}$. The processed materials were subsequently incorporated as cathodes in molten salt aluminum batteries and subjected to complete electrochemical discharge under consistent operational parameters (180°C , 5 mA g^{-1}). This systematic approach enabled direct evaluation of the EDCR method's universality across various cathode materials.

Figure 4a–c presents the discharge profile and phase evolution of an Al-NCM811 molten salt battery using spent NCM811 cathode material. The system delivered a discharge capacity of 718 mAh g^{-1} , which is close to its theoretical capacity, confirming efficient reconstruction of NCM811 (Figure 4a). Postdischarge XRD analysis (Figure 4b) revealed the complete disappearance of the (003) peak of the layered oxide at 18.8° , with new diffraction peaks appearing at 30.1° , 34.9° , 50.2° , 59.6° , and 62.5° , which are indexed to LiCl (PDF #04-0664). Additionally, weak peaks at 44.3° and 51.7° correspond to metallic Ni (PDF #89-7128), indicating nearly complete conversion of NCM811 into LiCl and Ni. Similarly, magnetic hysteresis measurements demonstrated that the originally nonmagnetic LCO cathode showed a significant increase in magnetization (saturation magnetization: $\approx 7.5 \text{ emu g}^{-1}$) after full discharge, which can be clearly attributed to the formation of ferromagnetic Ni nanoparticles (Figure 4c).

As shown in Figure 4d, the Al-NCA molten salt battery using spent NCA cathode material attained a discharge capacity of 790 mAh g^{-1} , which is near its theoretical capacity. XRD analysis (Figure 4e) revealed the disappearance of the original NCA (003) peak at 18.8° , with diffraction peaks at 30.1 , 34.9 , 50.2 , 59.6 , and 62.5° indexed to LiCl (PDF #04-0664), along with weaker peaks at 44.3° and 51.7° assigned to metallic Ni (PDF #89-7128). These results confirm the nearly complete conversion of NCA into LiCl and Ni, paralleling the reconstruction behavior seen in NCM811. Magnetic characterization (Figure 4f) further validated this transformation: The pristine NCA exhibited negligible magnetism (saturation magnetization $< 0.5 \text{ emu g}^{-1}$), while the discharged product displayed pronounced ferromagnetic properties (saturation magnetization $\approx 6 \text{ emu g}^{-1}$), consistent with the formation of Ni nanoparticles.

Similarly, the Al-LFP molten salt battery (Figure 4g) demonstrated a discharge capacity of 278 mAh g^{-1} , which is close to the theoretical capacity for LiFePO_4 . Postdischarge XRD analysis (Figure 4h) revealed the complete disappearance of the characteristic peaks of olivine-structured LFP, with new diffraction peaks at 44.7° and 65.0° corresponding to metallic Fe (PDF #01-1252) and LiCl (PDF #04-0664), respectively. This confirms the complete electrochemical decomposition of LiFePO_4 into Fe and LiCl. Magnetic hysteresis measurements (Figure 4i) further validated this transformation: The pristine LFP exhibited weak paramagnetic behavior (saturation magnetization $\approx 1.2 \text{ emu g}^{-1}$), while the discharged product displayed an eight-fold increase in saturation magnetization (9.5 emu g^{-1}). This significant enhancement in ferromagnetic properties is directly linked to the formation of metallic Fe nanoparticles, consistent with the EDCR mechanism observed in Co- and Ni-based cathodes.

2.4. Technoeconomic Analysis of Different Battery Recycling Technologies

As previously noted, the primary recycling processes for spent LIB cathode materials are pyrometallurgical recovery and hydrometallurgical recycling. In this section, we examine the economic and environmental impacts of our EDCR method compared to traditional pyrometallurgical and hydrometallurgical recovery technologies. First, from a technological process perspective,

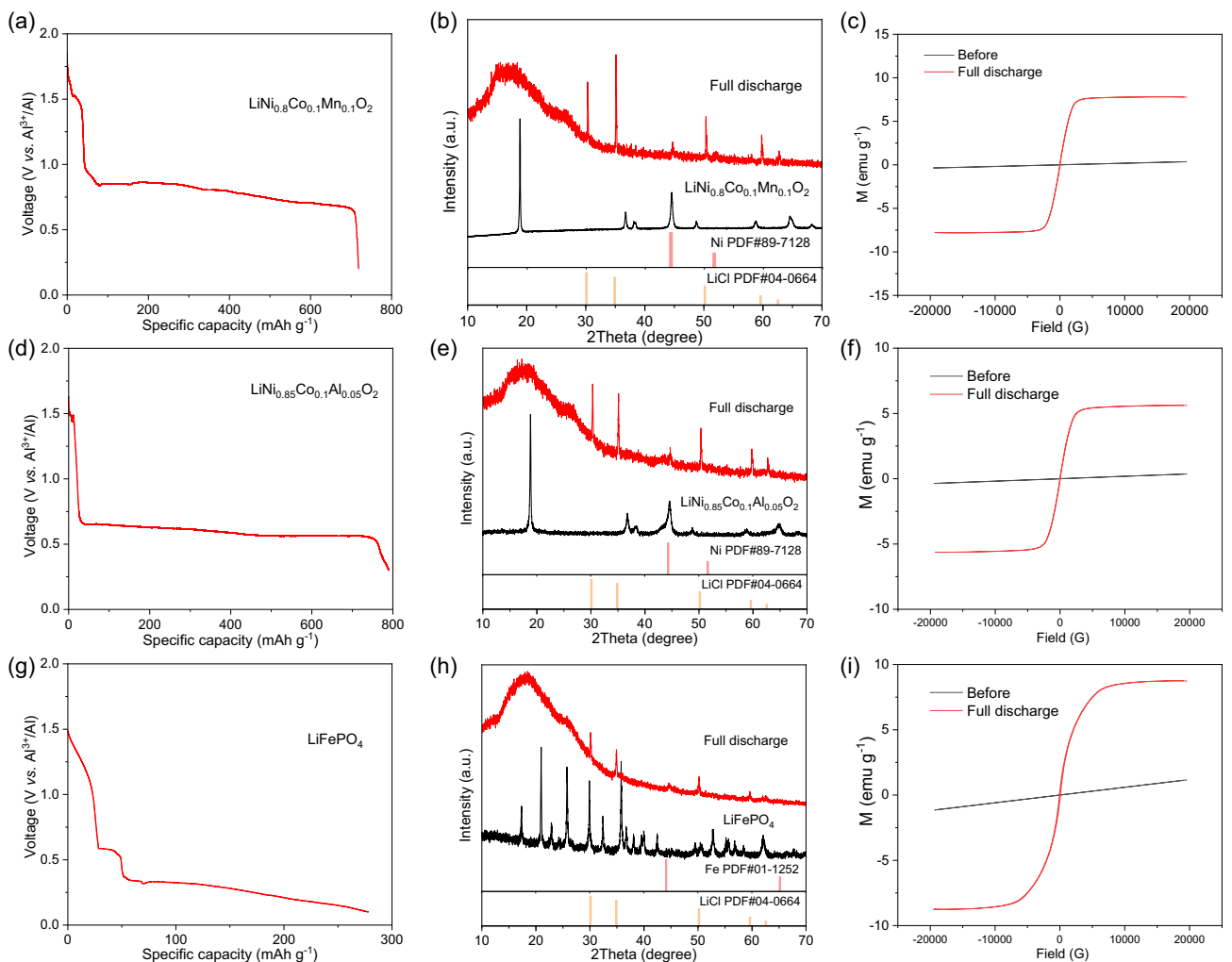


Figure 4. Wide adaption of the EDCR strategy for other spent cathode materials. a) Typical discharge curve of the Al-NCM811 battery at a temperature of 180 °C and a discharge current density of 5 mA g⁻¹. b) XRD pattern of the spent NCM811 after full discharge. c) Hysteresis loops of the spent NCM811 before and after full discharge. d) Typical discharge curve of the Al-NCA battery. The test was conducted at a temperature of 180 °C with a discharge current density of 5 mA g⁻¹. e) XRD pattern of the spent NCA after full discharge. f) Hysteresis loops of the spent NCA before and after full discharge. g) Typical discharge curve of the Al-LFP battery. The test was conducted at a temperature of 180 °C with a discharge current density of 5 mA g⁻¹. h) XRD pattern of the spent LFP after full discharge. i) Hysteresis loops of the spent LFP before and after full discharge.

hydrometallurgy involves dismantling spent batteries, followed by acid or alkali leaching of the spent cathode materials, precipitation, and filtration, ultimately yielding lithium or transition metal salts (Figure S12, Supporting Information). In contrast, pyrometallurgical recycling entails dismantling and crushing spent batteries, smelting the spent cathode materials to produce slag, and further refining to extract lithium or transition metal salts (Figure S13, Supporting Information). In our EDCR strategy, the spent cathode material is merely ball milled after the battery is dismantled, followed by a straightforward electrochemical discharge treatment, and the resulting product can be separated from the transition metal salts after simple washing and sintering (Figure S14, Supporting Information). Regarding total energy consumption, pyrometallurgical and hydrometallurgical recovery consumed 154.95 and 163.83 MJ kg⁻¹ of spent cells, respectively. The primary energy and material consumption in the pyrometallurgical recovery process stemmed from the high-temperature smelting phase, while in hydrometallurgy, most energy consumption was

associated with strong acid/alkali leaching and the extraction/precipitation of metals. In contrast, our EDCR strategy primarily consumes energy during the mechanical treatment of the materials, the temperature maintenance of the electrochemical process, and the final sintering process, resulting in a total energy consumption of ≈118.34 MJ kg⁻¹ of spent cells, which is over 20% lower than traditional hydrometallurgical and pyrometallurgical recovery methods (Figure 5a and Table S1, Supporting Information).^[9,26] Additionally, regarding greenhouse gas (GHG) emissions, the EDCR strategy resulted in GHG emissions of 7.21 kg kg⁻¹ of spent cells, which is slightly lower than those from hydrometallurgical recycling (11.17 kg kg⁻¹ of spent cells) and pyrometallurgical recycling (11.69 kg kg⁻¹ of spent cells) (Figure 5b). Finally, in terms of cost and profit, our EDCR strategy costs \$2.99 kg⁻¹ of spent cells, which is slightly lower than the costs of hydrometallurgical recycling (\$3.46 kg⁻¹) and pyrometallurgical recovery (\$3.47 kg⁻¹). However, because our EDCR strategy allows for reuse in multiple processes, it reduces material consumption and simplifies the

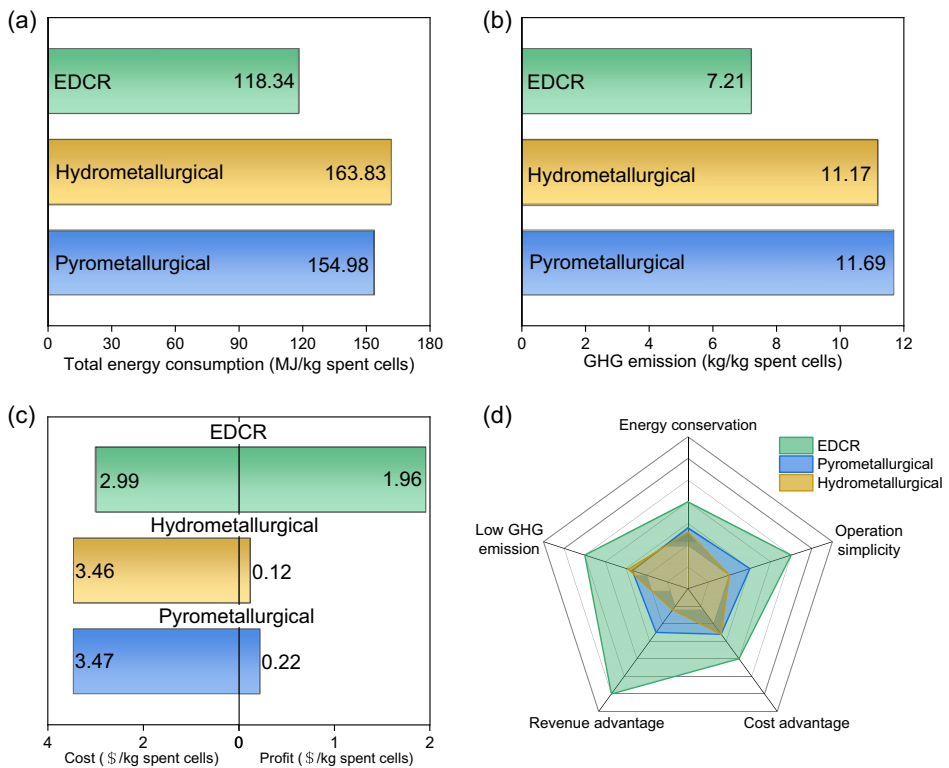


Figure 5. Environmental impact and economic analysis of the work. a) Total energy consumption; b) GHG emission; and c) cost and profit analysis of spent LIBs anode recycled by pyrometallurgical, hydrometallurgical, and our EDCR method. d) Comprehensive comparison of different battery recycling technologies.

operational process, offering significant advantages in environmental protection and energy savings (Table S2, Supporting Information).^[54–56] Consequently, the EDCR strategy achieved a profit margin of \$1.96 kg⁻¹ of spent cells, significantly higher than that of hydrometallurgical recovery (\$0.12 kg⁻¹) and pyrometallurgical recovery (\$0.22 kg⁻¹) (Figure 5c and Table S3, Supporting Information). These findings indicate that recovering lithium and transition metal salts from used LIBs through EDCR strategies can provide substantial environmental, energy, operational, and profit benefits, as summarized in Figure 5d.

3. Conclusion

In summary, we have developed an EDCR strategy in a tamed quaternary molten salt electrolyte for recycling the LIB cathode materials. By using spent cathode materials and Al current collector as cathode and anode electrodes, the assembled molten salt cells facilitated simple full discharge at 5 mA g⁻¹, 180 °C, enabling the complete reconstruction of the spent cathode materials. Consequently, the separation and recovery of a pure LiCl solution and a mixed solid of Co₃O₄ and Al₂O₃ from the LCO cathode material of spent batteries can be achieved with high efficiency, low cost, and at a large scale, which can be used to synthesize new cathode materials directly. Furthermore, universal experiments demonstrate that the EDCR strategy can effectively recover metals from the cathode electrodes of various spent LIBs, including NCM811, NCA, and LFP. Notably,

the EDCR strategy significantly minimizes resource loss during the recycling process, achieves high profits (\$1.96 kg⁻¹ of spent cells), lowers energy consumption by 23%, and effectively reduces GHG emissions (7.21 kg kg⁻¹ of spent cells), all while ensuring a streamlined workflow, reduced operational costs. Compared to traditional hydrometallurgical and pyrometallurgical methods, our proposed EDCR strategy exhibits strong competitiveness and offers a novel approach for exploring additional recycling technologies for spent battery cathode materials.

Supporting Information

The authors have cited additional references within the Supporting Information.

Acknowledgements

This work was supported by the National Key Research and Development Program of China (grant no. 2023YFB3809304), the Postdoctoral Fellowship Program of CPSF (GZB20230553), and the National Science Foundation of China (grant no. 52103329).

Conflict of Interest

The authors declare no conflict of interest.

Author Contributions

Yu Wang: data curation (lead); formal analysis (lead); and writing—original draft (lead). **Sicheng Feng:** data curation (equal); formal analysis (supporting); and writing—original draft (supporting). **Junling Huang:** data curation (equal) and writing—review editing (supporting). **Yuan Feng:** formal analysis (supporting) and writing—review editing (supporting). **Kai Luo:** formal analysis (supporting) and investigation (supporting). **Fang Liu:** data curation (supporting); formal analysis (supporting); and writing—review editing (supporting). **Shidong Li:** conceptualization (equal); data curation (supporting); and writing—review editing (supporting). **Xuanpeng Wang:** formal analysis (equal) and writing—review editing (equal). **Jiashen Meng:** conceptualization (lead); supervision (lead); writing—original draft (equal); and writing—review editing (lead).

Data Availability Statement

The data that support the findings of this study are available from the corresponding author upon reasonable request.

Keywords: aluminum batteries • complete reconstruction • lithium-ion batteries • molten salt electrochemistry • spent battery recycling

- [1] A. Manthiram, J. B. Goodenough, *Nat. Energy* **2021**, *6*, 323.
- [2] H. Ji, J. Wang, J. Ma, H.-M. Cheng, G. Zhou, *Chem. Soc. Rev.* **2023**, *52*, 8194.
- [3] A. Yoshino, *Angew. Chem. Int. Ed. Engl.* **2012**, *51*, 5798.
- [4] G. E. Blomgren, *J. Electrochem. Soc.* **2017**, *164*, A5019.
- [5] B. Huang, Z. Pan, X. Su, L. An, *J. Power Sources* **2018**, *399*, 274.
- [6] S. Chu, A. Majumdar, *Nature* **2012**, *488*, 294.
- [7] G. Harper, R. Sommerville, E. Kendrick, L. Driscoll, P. Slater, R. Stolkin, A. Walton, P. Christensen, O. Heidrich, S. Lambert, A. Abbott, K. Ryder, L. Gaines, P. Anderson, *Nature* **2019**, *575*, 75.
- [8] L. Mai, M. Yan, Y. Zhao, *Nature* **2017**, *546*, 469.
- [9] J. Lee, K. W. Park, I. Sohn, S. Lee, *Int. J. Minerals, Metall. Mater.* **2024**, *31*, 1554.
- [10] J. M. Tarascon, M. Armand, *Nature* **2001**, *414*, 359.
- [11] C. Tang, W. Shan, Y. Zheng, L. Zhang, Y. Liu, B. Liao, H. Chen, X. Hou, *Chem. Eng. J.* **2024**, *502*, 157578.
- [12] K. Kim, D. Raymond, R. Candeago, X. Su, *Nat. Commun.* **2021**, *12*, 6554.
- [13] E. Yoo, U. Lee, J. C. Kelly, M. Wang, *Resour., Conserv. Recycl.* **2023**, *196*, 107040.
- [14] A. M. Abdalla, M. F. Abdullah, M. K. Dawood, B. Wei, Y. Subramanian, A. T. Azad, S. Nourin, S. Afroze, J. Taweekun, A. K. Azad, *J. Energy Storage* **2023**, *67*, 107551.
- [15] S. Lee, A. Manthiram, *ACS Energy Lett.* **2022**, *7*, 3058.
- [16] M. Chen, X. Ma, B. Chen, R. Arsenault, P. Karlson, N. Simon, Y. Wang, *Joule* **2019**, *3*, 2622.
- [17] X. Ma, L. Azhari, Y. Wang, *Chem* **2021**, *7*, 2843.
- [18] B. K. Reck, T. E. Graedel, *Science* **2012**, *337*, 690.
- [19] Y. Zhao, Y. Kang, J. Wozny, J. Lu, H. Du, C. Li, T. Li, F. Kang, N. Tavajohi, B. Li, *Nat. Rev. Mater.* **2023**, *8*, 623.
- [20] J. Ordoñez, E. J. Gago, A. Girard, *Renewable Sustainable Energy Rev.* **2016**, *60*, 195.
- [21] J. Piątek, S. Afyon, T. M. Budnyak, S. Budnyk, M. H. Sipponen, A. Slabon, *Adv. Energy Mater.* **2021**, *11*, 2003456.
- [22] X. Zhang, L. Li, E. Fan, Q. Xue, Y. Bian, F. Wu, R. Chen, *Chem. Soc. Rev.* **2018**, *47*, 7239.
- [23] X. Zheng, Z. Zhu, X. Lin, Y. Zhang, Y. He, H. Cao, Z. Sun, *Engineering* **2018**, *4*, 361.
- [24] J. Neumann, M. Petranikova, M. Meeus, J.D. Gamarra, R. Younesi, M. Winter, S. Nowak, *Adv. Energy Mater.* **2022**, *12*, 2102917.
- [25] R. E. Ciez, J. F. Whitacre, *Nat. Sustainability* **2019**, *2*, 148.
- [26] J. C.-Y. Jung, P.-C. Sui, J. Zhang, *J. Energy Storage* **2021**, *35*, 102217.
- [27] J. J. Roy, N. Zaiden, M. P. Do, B. Cao, M. Srinivasan, *Joule* **2023**, *7*, 450.
- [28] J. J. Roy, B. Cao, S. Madhvani, *Chemosphere* **2021**, *282*, 130944.
- [29] T. Yang, D. Luo, A. Yu, Z. Chen, *Adv. Mater.* **2023**, *35*, 2203218.
- [30] Z. J. Baum, R. E. Bird, X. Yu, J. Ma, *ACS Energy Lett.* **2022**, *7*, 712.
- [31] J. Lin, E. Fan, X. Zhang, Z. Li, Y. Dai, R. Chen, F. Wu, L. Li, *Adv. Energy Mater.* **2022**, *12*, 2201174.
- [32] H. Zhang, Y. Ji, Y. Yao, L. Qie, Z. Cheng, Z. Ma, X. Qian, R. Yang, C. Li, Y. Guo, Y. Yuan, H. Xiao, H. Yang, J. Ma, J. Lu, Y. Huang, *Energy Environ. Sci.* **2023**, *16*, 2561.
- [33] V. Gupta, X. Yu, H. Gao, C. Brooks, W. Li, Z. Chen, *Adv. Energy Mater.* **2023**, *13*, 2203093.
- [34] Y. He, K. Jia, Z. Piao, Z. Cao, M. Zhang, P. Li, Z. Li, Z. Jiang, G. Yang, H. Xi, G. Zhou, W. Tang, Z. Qu, R. V. Kumar, S. Ding, K. Xi, *Angew. Chem. Int. Ed. Engl.* **2025**, *64*, e202422610.
- [35] F. Liu, S. Feng, J. Jiang, S. Li, X. Hong, J. Liu, L. Geng, L. Xu, X. Wang, J. Meng, *Cell Rep. Phys. Sci.* **2024**, *5*, 101894.
- [36] J. Wang, Y. Lyu, R. Zeng, S. Zhang, K. Davey, J. Mao, Z. Guo, *Energy Environ. Sci.* **2024**, *17*, 867.
- [37] M. Svärd, C. Ma, K. Forsberg, P. G. Schiavi, *ChemSusChem* **2024**, *17*, e202400410.
- [38] M. K. Tran, M.-T. F. Rodrigues, K. Kato, G. Babu, P. M. Ajayan, *Nat. Energy* **2019**, *4*, 339.
- [39] Z. Yuan, H. Liu, W. F. Yong, Q. She, J. Esteban, *Green Chem.* **2022**, *24*, 1895.
- [40] J. Wang, Q. Zhang, J. Sheng, Z. Liang, J. Ma, Y. Chen, G. Zhou, H.-M. Cheng, *Natl. Sci. Rev.* **2022**, *9*, nwac097.
- [41] E. A. Olivetti, G. Ceder, G. G. Gaustad, X. Fu, *Joule* **2017**, *1*, 229.
- [42] Q. Pang, J. Meng, S. Gupta, X. Hong, C. Y. Kwok, J. Zhao, Y. Jin, L. Xu, O. Karahan, Z. Wang, S. Toll, L. Mai, L. F. Nazar, M. Balasubramanian, B. Narayanan, D. R. Sadoway, *Nature* **2022**, *608*, 704.
- [43] G. Ding, M. Yao, J. Li, T. Yang, Y. Zhang, K. Liu, X. Huang, Z. Wu, J. Chen, Z. Wu, J. Du, C. Rong, Q. Liu, W. Zhang, F. Cheng, *Adv. Energy Mater.* **2023**, *13*, 2300407.
- [44] W. Weng, L. Tang, W. Xiao, *J. Energy Chem.* **2019**, *28*, 128.
- [45] Y. Zhong, Z. Li, J. Zou, T. Pan, P. Li, G. Yu, X. Wang, S. Wang, J. Zhang, *J. Hazard. Mater.* **2024**, *474*, 134794.
- [46] J. Meng, X. Hong, Z. Xiao, L. Xu, L. Zhu, Y. Jia, F. Liu, L. Mai, Q. Pang, *Nat. Commun.* **2024**, *15*, 596.
- [47] B.-R. Kim, G. Jeong, A. Kim, Y. Kim, M. G. Kim, H. Kim, Y.-J. Kim, *Adv. Energy Mater.* **2016**, *6*, 1600862.
- [48] G. Li, X. Lu, J. Y. Kim, J. P. Lemmon, V. L. Sprenkle, *J. Mater. Chem. A* **2013**, *1*, 14935.
- [49] G. Li, X. Lu, J. Y. Kim, V.V. Viswanathan, K. D. Meinhardt, M. H. Engelhard, V. L. Sprenkle, *Adv. Energy Mater.* **2015**, *5*, 1500357.
- [50] M. M. Li, X. Zhan, E. Polikarpov, N. L. Canfield, M. H. Engelhard, J. M. Weller, D. M. Reed, V. L. Sprenkle, G. Li, *Cell Rep. Phys. Sci.* **2022**, *3*, 100821.
- [51] C. Lin, J. Li, Z.-W. Yin, W. Huang, Q. Zhao, Q. Weng, Q. Liu, J. Sun, G. Chen, F. Pan, *Adv. Mater.* **2024**, *36*, 2307404.
- [52] M. Wang, K. Liu, S. Dutta, D. S. Alessi, J. Rinklebe, Y. S. Ok, D. C. W. Tsang, *Renewable Sustainable Energy Rev.* **2022**, *163*, 112515.
- [53] J. Hao, J. Hao, D. Liu, L. He, X. Liu, Z. Zhao, T. Zhao, W. Xu, *J. Hazard. Mater.* **2024**, *472*, 134472.
- [54] L. Reinhart, D. Vrucak, R. Woeste, H. Lucas, E. Rombach, B. Friedrich, P. Letmathe, *J. Cleaner Prod.* **2023**, *416*, 137834.
- [55] A. Cornelio, A. Zanoletti, E. Bontempi, *Curr. Opin. Green Sustainable Chem.* **2024**, *46*, 100881.
- [56] Y. Yao, M. Zhu, Z. Zhao, B. Tong, Y. Fan, Z. Hua, *ACS Sustainable Chem. Eng.* **2018**, *6*, 13611.

Manuscript received: February 17, 2025

Revised manuscript received: April 3, 2025

Version of record online: April 4, 2025